atmosphere

MDPI

Article

Increase in the Intensity of Air–Sea Coupling in the Key ENSO Region during 1955–2020

Zhiqing Liu [1,2] and Jianjun Xu [1,3,*]

[1] CMA-GDOU Joint Laboratory for Marine Meteorology, South China Sea Institute of Marine Meteorology, Guangdong Ocean University, Zhanjiang 524088, China
[2] College of Ocean and Meteorology, Guangdong Ocean University, Zhanjiang 524088, China
[3] Shenzhen Institute, Guangdong Ocean University, Shenzhen 518000, China
* Correspondence: jxu@gdou.edu.cn

Abstract: The El Niño and Southern Oscillation (ENSO), a phenomenon of air–sea coupling in the tropical Pacific, has strong response to global climate change. In this study, the primary region where ENSO occurred during the period 1955–2020 was selected as the key ENSO region, and the changes in air–sea coupling in this region were explored. The New Southern Oscillation Index (NSOI), modified from the previous Southern Oscillation Index, represents atmospheric changes, and the Niño-3.4 index represents oceanic changes. The absolute value of the running correlation coefficient between the Niño-3.4 index and NSOI in the 121-month time window was defined as the Intensity of Air–Sea Coupling (IASC) in the key ENSO region. The results showed that the IASC has significantly increased, with a confidence level of 95%, during the period 1955–2020, and the range where the correlation coefficient between the Niño-3.4 index and the sea level pressure anomaly over the key ENSO region was greater than 0.6 has evidently expanded in the context of global warming, which corresponded to the increase in IASC. Moreover, the coupling positions of sea surface temperature and wind anomalies changed, tending to the east of the equatorial Pacific during 1977–1998, and to the west during 1999–2020.

Keywords: global warming; El Niño and Southern Oscillation; air–sea coupling

check for updates

Citation: Liu, Z.; Xu, J. Increase in the Intensity of Air–Sea Coupling in the Key ENSO Region during 1955–2020. *Atmosphere* **2022**, *13*, 2025. https://doi.org/10.3390/atmos13122025

Academic Editor: Jimy Dudhia

Received: 11 October 2022
Accepted: 28 November 2022
Published: 1 December 2022

1. Introduction

According to the Working Group 1 contribution to the Sixth Assessment Report of the Intergovernmental Panel on Climate Change [1], the global surface temperature during 2011–2020 was 1.09 °C higher than that during 1850–1900. Many of the changes observed in the climate system have been unprecedented for thousands of years, and some have been irreversible for hundreds to thousands of years. Lin and Franzke found rapid warming in 1920–1945 and 1977–2000, with a hiatus in 1946–1976 and 2001–2013 [2]. Dong and McPhaden indicated that the global warming hiatus of the early 20th century was temporary, and that temperatures during that period were still much higher than before [3]. These studies suggest that global warming is still significant, and that its effects on the climate system deserve continued attention. Therefore, it is necessary to thoroughly study the changes in the climate system under global warming to lay a better theoretical foundation for coping with possible extreme weather and climate in the future.

The El Niño and Southern Oscillation (ENSO) is the strongest interannual fluctuation in the tropical Pacific [4]. Owing to the extensive and far-reaching impacts of ENSO on weather, climate, and social economy [5–8], its development mechanisms and change characteristics are key points in meteorology. El Niño (La Niña) events are primarily characterized by a continuous warm (cold) anomaly of sea surface temperature (SST) in the eastern or central equatorial Pacific. The Southern Oscillation (SO) refers to the oscillating sea level pressure (SLP) between the eastern and western tropical Pacific. Bjerknes pointed out that El Niño and SO originate from the same large–scale ocean–atmosphere interaction phenomenon in the tropical Pacific [9]. The warm SST anomalies in the eastern equatorial Pacific reduce the east–west SST gradient, resulting in the weakening of the Walker circulation and negative (positive) SLP anomalies in the eastern (western) tropical Pacific. In turn, westerly anomalies alter ocean circulation and strengthen SST anomalies. Thus, the ENSO is a coupled system of the tropical ocean and atmosphere. In this study, the primarily region where El Niño and SO occurred from 1955 to 2020 is defined as the key ENSO region; namely, the tropical Pacific and eastern tropical Indian Ocean (30° N–30° S, 60° E–80° W).

In recent decades, numerous achievements have been made in ENSO research [10–17]. The change in ENSO under global warming has become a concern for many scholars, who have found that the change in the climate background state drives the change in ENSO characteristics. Vecchi et al. pointed out that the intensity of ENSO may change because the average state of the atmosphere and ocean changes with global warming [18]. Deng et al. found that when CO_2 increased, the frequency of modeled ENSO varied, influenced by the different responses of tropical Pacific climate background states to CO_2 increases in different models [19]. Philip and Van Oldenborgh found that, against the background of global warming, the depth of the mean thermocline becomes shallow in the tropical Pacific, which increases the sensitivity of the SST response to wind anomalies [20]. Kim and Jin used multimodal data from the Third Coupled Model Comparison Program (CMIP3) and suggested that warming can change the average state and increase the sensitivity of the ocean–atmosphere response, thereby strengthening the Bjerknes feedback and increasing ENSO instability [21]. Chen et al. obtained similar conclusions using multimodal data [22]. Cai et al. used the multimodal data from CMIP5 to compare the situation of the 20th century with that of the next warmer century in the equatorial Pacific, and found that the ocean surface layer will warm more rapidly than the subsurface layer, leading to enhanced stratification of the upper ocean, shallow thermocline, and a strengthening of the coupling between wind and ocean, thus increasing ENSO instability [23]. Xia et al. indicated that different warming locations in the tropical Pacific would lead to different position changes in low-level trade wind intensity, which in turn would change the location of the strongest air–sea coupling [24].

Based on the above historical studies, one can conclude that changes in the climate background state under warming can affect the occurrence and development of ENSO by changing the strength and position of air–sea coupling. Therefore, it is important to study the changes in the air–sea coupling process in the context of warming to predict the future trend of ENSO characteristics. However, previous studies in this field have been mostly based on models, and few studies could provide an intuitive representation of the coupling strength between the atmosphere and the ocean.

Considering that SLP is an important variable of the ENSO phenomenon, which has a direct response to SST changes, and its anomalies are important driving forces of atmospheric circulation, we used the running correlation results of SST and SLP characteristic indices to characterize the air–sea coupling strength in the key ENSO region. Moreover, some historical reanalysis data were combined to show the intensity and location changes in air–sea coupling in the key ENSO region during 1955–2020.

The main study period was 1955–2020. The data and methods, particularly the definition methods of the New Southern Oscillation Index (NSOI) and the Intensity of Air–Sea Coupling (IASC), are described in Section 2. Sections 3 and 4 discuss the variation in the spatial and temporal distribution characteristics of the coupling between the atmosphere and the ocean in the key ENSO region. We present a summary and discussion in Section 5.

2. Data and Methods

2.1. Data

The monthly mean SST for 1955–2020 was obtained from the National Oceanic and Atmospheric Administration (NOAA) Extended Reconstructed Sea Surface Temperature version 5 (ERSST v5), with a spatial resolution of 2° × 2° [25]. The monthly mean SLP of Tahiti station (17.9° S, 148.1° W) and Darwin station (12.3° S, 131° E), as well as the Niño-3.4 index during 1950–2020, were obtained from the NOAA Climate Prediction Center [26]. The Niño-3.4 index was calculated from the three-month moving average of SST anomalies in the Niño-3.4 region of the ERSST v5 dataset. Grid data of monthly mean SLP, air temperature at sigma level 0.995, and sea surface wind (SSW) from the National Centers for Environmental Prediction and National Center for Atmospheric Research (NCEP/NCAR) reanalysis version 1 were used in this study, with a spatial resolution of 2.5° × 2.5°, spanning 1950–2020 [27]. The monthly mean 0–2000 m ocean heat content (OHC) anomalies from 1955 to 2020, with a spatial resolution of 1° × 1°, were obtained from the Institute of Atmospheric Physics [28]. Prior to correlation analysis in this study, the linear trends of the data used were removed to ensure the consistency of data processing.

2.2. Singular Value Decomposition

The original fields of the two variables in singular value decomposition (SVD) [29–31] are called the left and right fields, and the extracted modes are called the left and right singular vectors, respectively. The singular vectors of the same original field are orthogonal to each other. The first mode of SVD consists of the first left and right singular vectors together with their respective time coefficients. This method was used to study the synergistic relationship between the SST and the SSW anomaly fields. In addition, the correlation coefficient between the original field of SVD and the time series corresponding to a certain singular vector of another original field is called the heterogeneous correlation map, and its large values indicate the key influence region of one field to another. This method was used to determine the key influence area of the SLP anomaly field on the SST anomaly field in this study.

2.3. Definition of the Three Periods during Global Temperature Change

In recent decades, there have been dramatic changes in global temperature. Figure 1 shows the annual average change curves of the OHC at 0–2000 m, SST, and the near-underlying surface air temperature in the global and tropical Pacific from 1955 to 2020. Both ocean and atmosphere show a fluctuating increase in temperature. From 1955 to 2020, the global mean OHC at 0–2000 m increased by approximately 1.05 × 109 J/m^2, SST increased by approximately 0.73 °C, and the near-underlying surface air temperature increased by approximately 1.44 °C. In the tropical Pacific, the OHC at 0–2000 m and the near-underlying surface air temperature increased slightly less than the global average, whereas the increase in SST was similar.

On the decadal scale, Pacific Decadal Oscillation (PDO) is the leading mode of the internal SST variability and a signal to reveal the Pacific climate background, playing an important role in modulating ENSO and its effects [32,33]. Considering that the phase of PDO changed in both 1976–1977 and 1998–1999 [32], we selected them to evenly divide the period from 1955 to 2020 into three periods in order to analyze the temperature background. In terms of the linear trends of different time periods, the periodic changes in global and tropical Pacific temperatures were similar, showing that the temperature was constant from 1955 to 1976 (period 1), slowly increased from 1977 to 1998 (period 2), and sharply increased from 1999 to 2020 (period 3). In the latter part of the article, the changes in the coupling characteristics between atmospheric and oceanic variables were studied in these three periods against the background of continuous warming.

2.4. Definition of NSOI

The strength of the SO is traditionally characterized by the Southern Oscillation Index (SOI, https://www.ncei.noaa.gov/access/monitoring/enso/so (accessed on 1 September 2022)), which is the standardized anomaly of the difference between the standardized Tahiti SLP and the standardized Darwin SLP. Figure 2 shows the spatial distribution of winter SST and SLP anomalies in ENSO events during the three periods from 1955 to 2020. It can be seen that the SST and SLP anomalies caused by ENSO are mainly located in the tropical

Pacific and eastern tropical Indian Ocean (30° N–30° S, 60° E–80° W), which is the key ENSO region in this study. It is clear from Figure 2 that the single-station SLP anomalies at Tahiti (right asterisk) and Darwin (left asterisk) cannot accurately characterize the regional SLP anomalies in the eastern and western tropical Pacific. Shi and Su also argued this, and used ERA-Interim data from 1980 to 2017 to prove that the area-averaged SLP is more representative than a single site [34]. Therefore, it is necessary to select more appropriate regions to characterize SLP anomalies. In this study, a NSOI is defined that shows a good correlation with the Niño-3.4 index, which is more advantageous than the SOI. The specific method of definition is as follows.

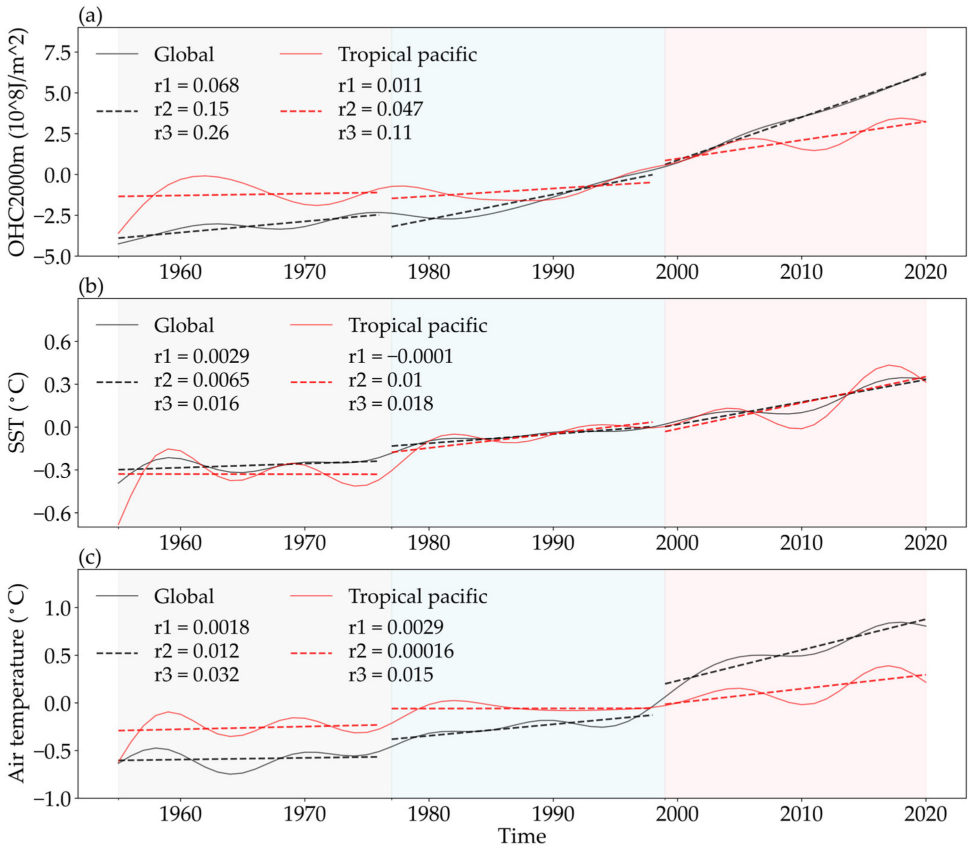

Figure 1. The annual mean series of (**a**) 0–2000 m ocean heat content anomalies, (**b**) sea surface temperature (SST) anomalies, and (**c**) air temperature anomalies at sigma level 0.995. The time series are low-pass filtered for 10 years to retain the decadal variation signal. The black solid line is the global average abnormal values and the red is the area-average abnormal values of the tropical Pacific (30° N–30° S, 120° E–80° W). The abnormal values are calculated using 1981–2010 as the mean climate state. The dashed lines of the three periods are the linear trends of 1955–1976 (p1; gray background), 1977–1998 (p2; blue background), and 1999–2020 (p3; pink background), respectively. The r1, r2, and r3 are the corresponding linear regression coefficients.

To identify the SLP anomaly regions that are most closely related to SST changes, the SST and SLP anomaly fields were treated with SVD. A heterogeneous correlation map between the original SLP anomaly field and the time coefficient series corresponding to the SVD first mode of the SST anomaly field was used to define the key SLP regions. The monthly mean SLP values were obtained from NCEP/NCAR reanalysis version 1. Figure 3 shows the heterogeneous correlation map. The high correlation areas represent the key influence regions of SLP anomalies on SST anomalies, and are primarily located in the left black box area A (10° N–20° S, 90° E–160° E) and the right black box area B (10° N–20° S, 150° W–80° W). These two regions were selected as the key SLP regions, and the NSOI was defined as the standardized anomaly of the difference between the standardized area-average monthly SLP in areas B and A.

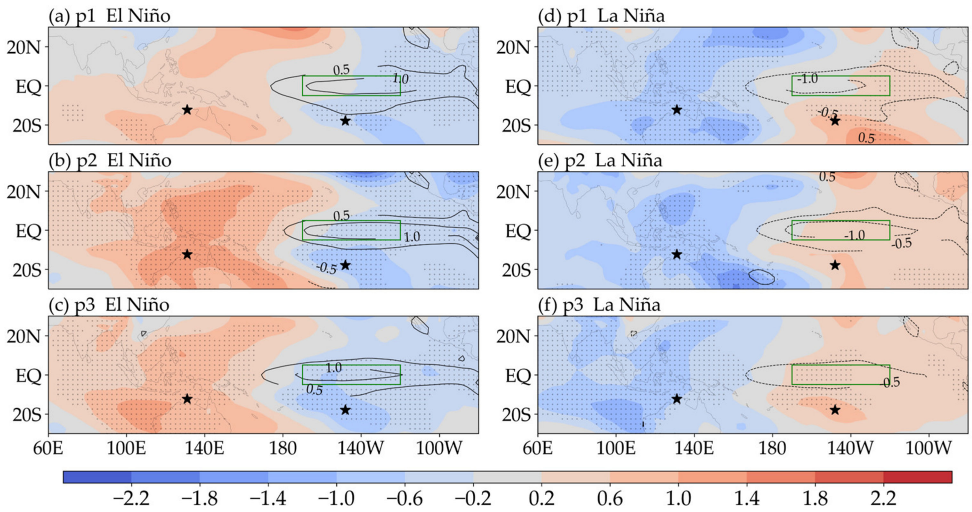

Figure 2. Composite results of SST anomalies (°C; isoline) and sea level pressure (SLP) anomalies (hPa; shade) averaged over December–February of ENSO in three periods during 1955–2020, namely, boreal winters of El Niño events (**a**) 1957, 1963, 1965, 1968, 1972, 1976, (**b**) 1977, 1979, 1982, 1986, 1991, 1994, 1997, (**c**) 2002, 2004, 2006, 2009, 2015, 2018, 2019, and boreal winters of La Niña events (**d**) 1955, 1964, 1970, 1973, 1975, (**e**) 1984, 1988, 1995, (**f**) 1999, 2000, 2007, 2010, 2011, 2017, 2020. The SST and SLP retain ENSO signals for 2–7 years by band-pass filtering. The black solid (dashed) isolines represent positive (negative) SST anomalies. The p1, p2, and p3 are the same as in Figure 1. The green box is the Niño-3.4 region. The left and right asterisks in each subfigure show the locations of the Darwin and Tahiti stations, respectively. Light black dots indicate that the composite results pass the Student *t*-test with a confidence level of 95%.

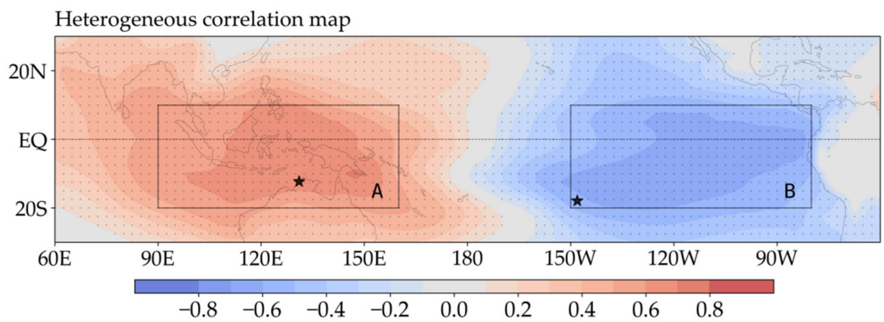

Figure 3. The correlation coefficients (shade) between the original SLP anomaly field and the time coefficient series corresponding to the singular value decomposition (SVD) first mode of the SST anomaly field during 1955–2020. The black solid box A and B are the key SLP regions selected in this study. The left and right asterisks show the locations of the Darwin and Tahiti stations, respectively. Light black dots indicate that the results pass the Student *t*-test with a confidence level of 95%.

For comparison, other SO indices were recalculated using SLP from NCEP/NCAR reanalysis version 1, using established methodologies. To compare the representative difference between area-averaged SLP and single-grid SLP, two SO indices were established by referring to the method of Shi and Su [34]. The standardized anomaly of the difference between the standardized SLP of the grid point (17.5° S, 147.5° W) near Tahiti station and the standardized SLP of the grid point (12.5° S, 130° E) near Darwin station was defined as SOIs. Furthermore, the standardized anomaly of the difference between the standardized mean SLP of the regions covering Tahiti (12.5° S–22.5° S, 170° W–130° W) and Darwin (7.5° S–17.5° S, 110° E–150° E) was defined as SOIm. The Equatorial Oscillation Index (EOI) is defined as the standardized anomaly of the difference between the standardized mean SLP of the areas over the eastern equatorial Pacific (5°N–5°S, 150°W–130°W) and Indonesia (5° N–5° S, 110° E–130° E) [34]. The Equatorial Southern Oscillation Index (EQ-SOI) is defined as the standardized anomaly of the difference between the standardized mean SLP of the areas over the eastern equatorial Pacific (5° N–5° S, 130° W–80° W) and Indonesia (5° N–5° S, 90° E–140° E) (http://iridl.ldeo.columbia.edu/maproom/ENSO/Time_Series/Equatorial_SOI (accessed on 1 September 2022)).

Generally, when the SST anomalies in the Niño-3.4 region are positive, the SLP over the central and eastern Pacific decreases, whereas the SLP over Indonesia increases, and the SO index is negative. Therefore, the SO index is generally negatively correlated with the Niño-3.4 index. To directly reflect the synergistic relationship between the two indexes, the time series of the SO index and Niño-3.4, as well as the absolute value of their correlation coefficients from 1950 to 2020, are shown in Figure 4. Compared with SOIs, SOIm has a higher correlation with Niño-3.4, indicating that the representation of area-averaged SLP is better than that of a single-grid SLP. Compared with SOIs and SOIm, it is noticeable that EOI, EQ-SOI, and NSOI have higher correlations with Niño-3.4, indicating that SLP anomalies near the tropical equator are closely related to SST anomalies. Compared with other SO indices, NSOI has the highest correlation with Niño-3.4, which indicates that NSOI has a prominent advantage in reflecting SLP changes associated with SST anomalies in the key ENSO region. Therefore, we used NSOI instead of other SO indices in this study.

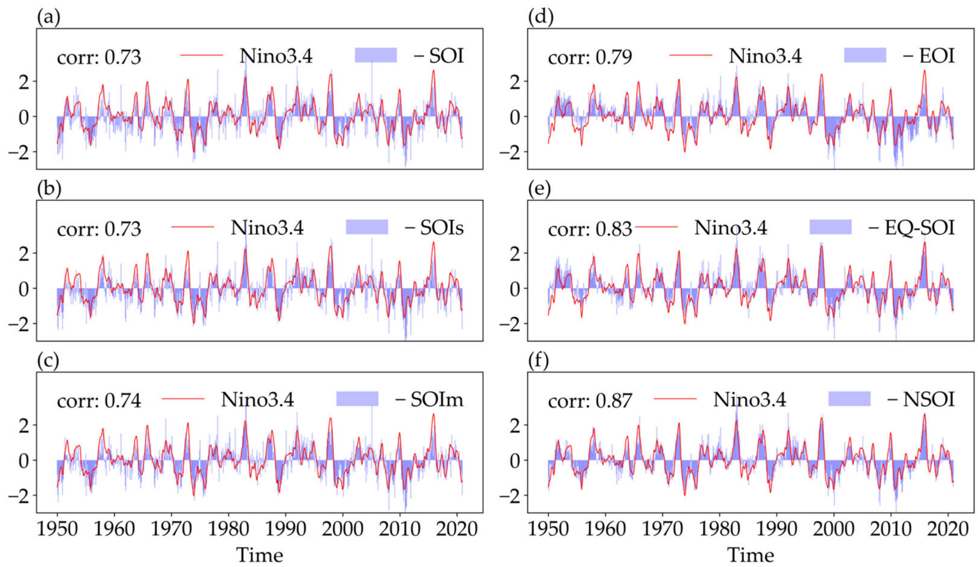

Figure 4. Time series of Niño-3.4 index (°C; red line) and Southern Oscillation (SO) indexes (blue bar): (**a**) SOI, (**b**) SOIs, (**c**) SOIm, (**d**) EOI, (**e**) EQ-SOI, and (**f**) NSOI during 1950–2020. The number following 'corr:' is the absolute value of the correlation coefficient between Niño-3.4 index and SO index in the corresponding subfigure.

2.5. Expression of Air–Sea Coupling Strength

The SST and SLP fields are a pair of important physical variable fields that can reflect the ENSO air–sea interaction. Therefore, a new parameter, the IASC, is defined in this study to reflect the covariation between the ocean and atmosphere, and to characterize the air–sea coupling strength in the key ENSO region. The specific method Sof definition is as follows.

According to the above analysis in the key ENSO region, the Niño-3.4 index and NSOI can accurately characterize SST and SLP anomalies, respectively. Because the running correlation can reflect the degree of similarity between the change trends in the two groups of sequences [35], the absolute value of the correlation coefficient of Niño-3.4 and NSOI was calculated by taking 121 months as the running window and defined as IASC to show the intensity of their interdecadal synergistic change.

3. Trend of Air–Sea Coupling Strength

This is based on the coupling of SST and SLP to analyze the variation in the air–sea coupling intensity in the key ENSO region.

First, the variation of IASC with time is shown in Figure 5. Note that the IASC values are all greater than 0.7, indicating that the ocean and atmosphere in the key ENSO region maintain a good synergistic change relationship. In addition, the IASC shows fluctuating changes and an increasing trend with time from 1955 to 2020, that, to some extent, indicates that the air–sea coupling strength in the key ENSO region is increasing in the context of warming.

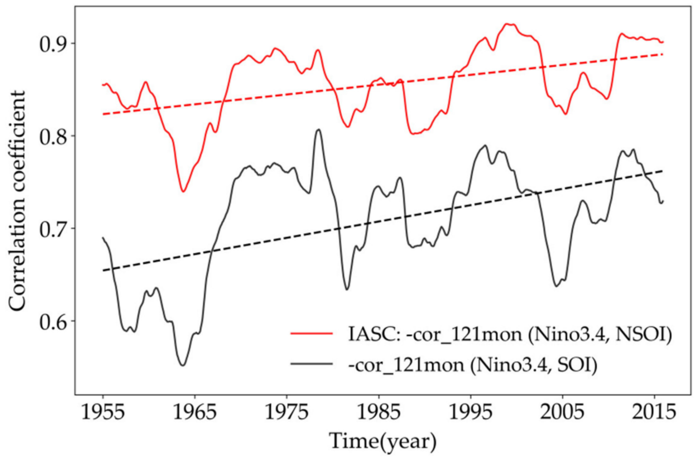

Figure 5. The red solid line shows the change in the Intensity of Air–Sea Coupling (IASC). IASC is defined as the absolute value of the 121-month running correlation coefficient between Niño-3.4 index and NSOI. The black solid line shows the change in the absolute value of the 121-month running correlation coefficient between Niño-3.4 index and SOI. The dashed lines are the corresponding linear trends. All the results pass the Student *t*-test with a confidence level of 95%.

For the same running calculation when SOI is used to characterize the SLP anomalies, the results are shown as a black curve in Figure 5. It is evident that the correlation intensity is much lower than that of the IASC, which also indicates that the NSOI has a greater advantage in characterizing SLP changes.

Second, to study the spatial distribution of the differences in air–sea coupling within the key ENSO region during different temperature periods, Niño-3.4 index sequences were correlated with SLP anomaly fields, and the results are shown in Figure 6. Overall, the Niño-3.4 index is significantly negatively correlated with SLP anomalies in the eastern tropical Pacific, but positively correlated with SLP anomalies in Indonesia and the nearby regions. The main coupling region is within the black dashed-box area (30° N–30° S, 60° E–80° W) in Figure 6, which corresponds to the key ENSO region.

According to the statistical analysis in the previous section, the global and tropical Pacific temperatures were relatively stable in period 1, slowly increased in period 2, and sharply increased in period 3. Comparing the different time periods in Figure 6, it can be seen that the correlation coefficients between Niño-3.4 and SLP anomalies have changed at some spatial points. Further statistics are presented below to demonstrate the coupling differences.

Figure 7 shows the size of the area corresponding to every 0.01 correlation intensity in the above main coupling region. Compared with period 1, the area with positive correlations greater than 0.3 in period 2 is evidently enlarged. Compared with that in periods 1 and 2, more area has high correlation intensity in period 3. In particular, the range of correlation coefficients greater than 0.6 is evidently expanded. Therefore, we inferred that the area of strong coupling between SST and SLP increases with warming.

This indicated that, to some extent, global warming is accompanied by a strengthening of air–sea coupling in the key ENSO region.

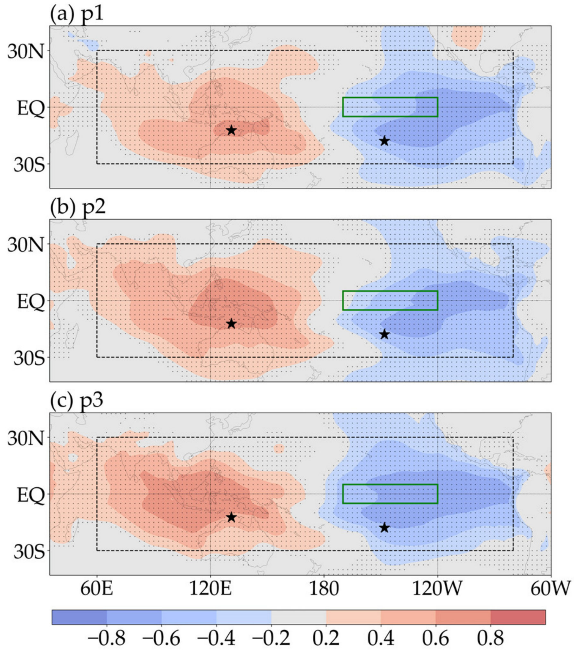

Figure 6. The correlation coefficients (blue-red scale) between Niño-3.4 index series and SLP anomaly field during three periods (**a**–**c**). The p1, p2, and p3 are the same as in Figure 1. The green box is the Niño-3.4 region. The left and right asterisks in each subfigure show the locations of Darwin and Tahiti stations, respectively. The black dashed box is the main coupling region between Niño-3.4 index and SLP anomalies. Light black dots indicate that the results pass the Student *t*-test with a confidence level of 95%.

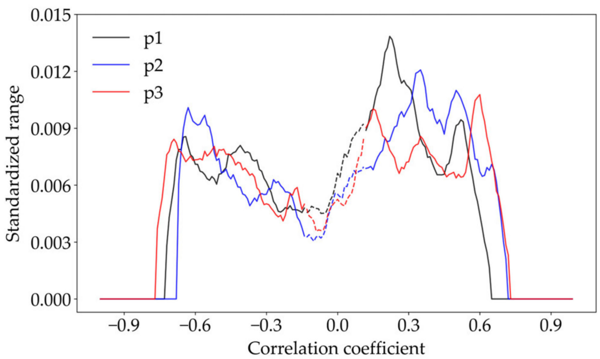

Figure 7. The standardized range corresponding to every 0.01 correlation intensity in the main coupling region between Niño-3.4 index series and SLP anomaly field (black dashed box in Figure 6). The standardized results are smoothed by nine equal weights. The p1, p2, and p3 are the same as in Figure 1. Solid (dashed) lines indicate passing (failing) the Student *t*-test with a confidence level of 95%.

4. Changes in Coupling between SST and SSW

The pressure gradient is an important driving force for air movement, and SLP anomalies are closely related to SSW anomalies. The above study indicates that the coupling between SST and SLP anomalies changes with warming; therefore, it is speculated that the coupling between SST and SSW may also accordingly change. Figure 8a,c,e shows the first spatial mode of SVD of the SST and SSW anomaly fields during three periods, and Figure 8b,d,f shows the corresponding time coefficient series. The covariance contribution rates of the first mode of SVD during three periods are greater than 80%, indicating that the first mode can reflect the relationship of the synergistic change between the two variable fields.

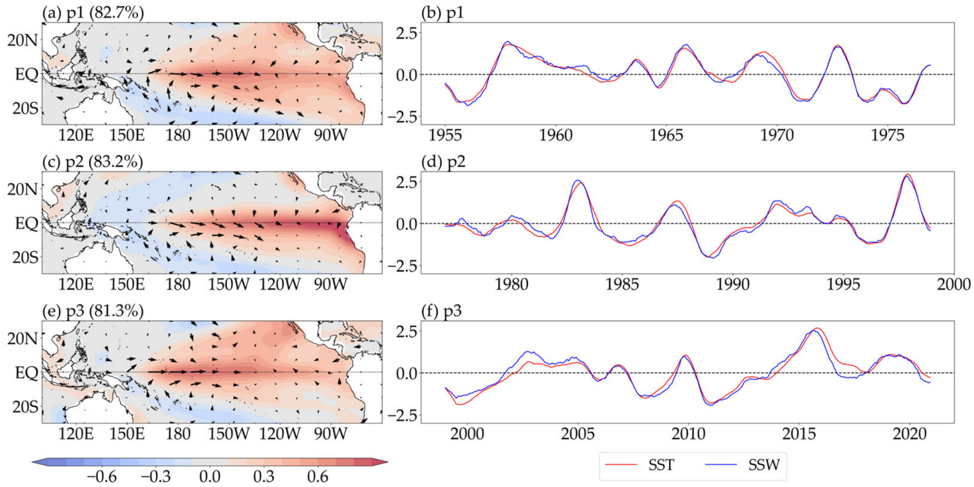

Figure 8. The SVD first spatial mode of SST anomalies (blue-red scale) and sea surface wind (SSW) anomalies (arrows) during three periods (**a**,**c**,**e**) and their corresponding time coefficient series (**b**,**d**,**f**). The p1, p2, and p3 are the same as in Figure 1. The percentages in parentheses (**a**,**c**,**e**) indicate the covariance contribution rates of the first mode.

By comparing the coupling differences during three periods in Figure 8, the following features can be observed. First, the primarily coupling positions of SST and SSW anomalies were shifted to the east of the equatorial Pacific in period 2, and to the west in period 3. Second, when the SST anomalies were positive in the coupling region, anomalous westerlies in periods 1 and 3 and anomalous northwesterlies in period 2 were observed. Third, the large-value regions of SSW anomalies were primarily located in the south of the central tropical Pacific in period 1, concentrated around the equator in period 2, and tended to the north-west in period 3.

To more directly reflect the spatial variation of the coupling strength between SST and SSW, the correlation analysis was conducted between the Niño-3.4 index and zonal SSW anomaly field in each period, and the results are shown in Figure 9. The positive correlation indicates that anomalous zonal sea surface westerly (easterly) wind occurs when the Niño-3.4 index is positive (negative). A high positive correlation indicates strong coupling between SST and zonal SSW. The main coupling region is within the black dashed-box area (10° N–10° S, 130° E–120° W), as shown in Figure 9. Although the strong coupling positions during three periods appear near the dateline of the central equatorial Pacific, those positions tend to the east in period 2, and to the west in period 3.

Figure 10 shows the proportion of the area occupied by different positive correlation intensities within the black dashed box in Figure 9. It can be found that the proportions of the areas with correlation intensities greater than 0.2, 0.6, and 0.8 all increase with time, indicating that the synergy between the Niño-3.4 index and zonal SSW of the central equatorial Pacific is improving in the context of warming.

These results show that the coupling locations of SST and SSW are different under different temperature conditions, and that the coupling becomes stronger in the key ENSO region in the context of warming.

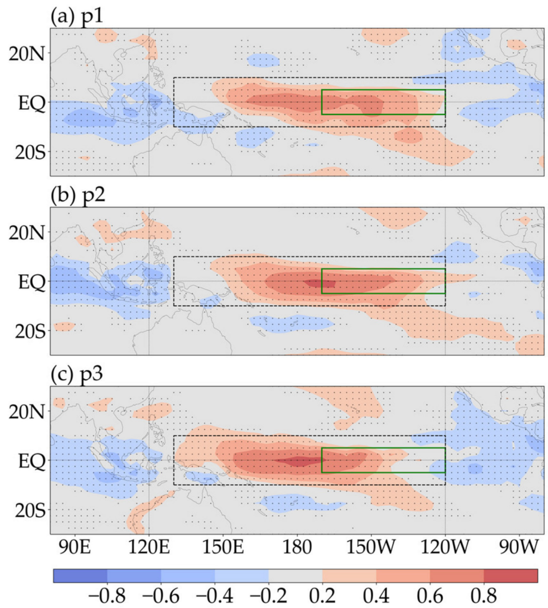

Figure 9. The correlation coefficients (blue-red scale) between the Niño-3.4 index series and zonal SSW anomaly field during the three periods (**a**–**c**). The p1, p2, and p3 are the same as in Figure 1. The green box is the Niño-3.4 region. The black dashed box is the main coupling region between the Niño-3.4 index and zonal SSW anomalies. Light black dots indicate that the results pass the Student *t*-test with a confidence level of 95%.

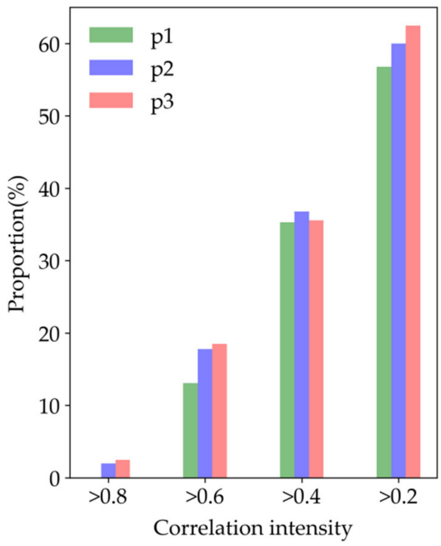

Figure 10. The proportion of the different correlation intensities between the Niño-3.4 index and zonal SSW anomaly field in the main coupling region (black dashed box in Figure 9). The p1, p2, and p3 are the same as in Figure 1.

5. Summary and Discussion

In this study, a new SO index, the NSOI, was defined to characterize the SLP oscillation in the key ENSO region. Compared with the other SO indices, NSOI showed a better synergistic relationship with the Niño-3.4 index (correlation coefficient of −0.87). Furthermore, the absolute value of the 121-month running correlation coefficient between Niño-3.4 and NSOI, defined as IASC, robustly increased in the context of increased warming from 1955 to 2020.

Next, we compared the spatial distribution of coupling between ocean and atmospheric variables during three periods of stable (1955–1976), slowly increasing (1977–1998), and rapidly increasing (1999–2020) global temperatures. The main characteristics of these changes are as follows. First, with intensified warming, the range where the correlation coefficient between the Niño-3.4 index and the SLP anomaly is greater than 0.6 and the corresponding strong correlation area between the Niño-3.4 index and the zonal SSW anomaly field have evidently expanded over the key ENSO region. In other words, they become more synergistic, indicating that the coupling between the ocean and atmosphere is strengthened in the key ENSO region, which corresponds to an increase in IASC. Second, the coupling positions of SST and SSW anomalies changed, tending to the east of the equatorial Pacific in period 2, and to the west in period 3. Moreover, the anomalous SSW shifted to the north–west side of the central equatorial Pacific during 1955–2020.

The above air–sea coupling changes occurred in the context of increased warming, but whether they can be attributed to global warming requires further study. Combined with previous studies on the changes in the mean state and ENSO characteristics under global warming, we find some directions may be suitable for studying the mechanisms of air–sea coupling changes.

In both CMIP3 and CMIP5 results, the climatological thermocline in the equatorial Pacific becomes shallow under global warming [36,37], demonstrating that the isotherm vertical displacements within the thermocline depth can more easily influence the SST. Philip and Van Oldenborgh [20] studied the shifts in ENSO couplings by climate models, and found that shallower thermocline and mixed layer depths can increase SST sensitivity to the changes in thermocline and wind stress. From 1955 to 2020, the global average temperature rose (as shown in Figure 1), so we speculate that the increase in the intensity of air–sea coupling in the decadal variation may be related to the change in thermocline depth under warming conditions.

Behera and Yamagata [38] suggested that a warmer tropical Pacific and a flatter thermocline seem to favor frequent El Niño Modoki (also called central Pacific El Niño), characterized by the shift of the center of the SST anomaly to the central Pacific compared to traditional El Niño [39,40]. In the last two decades, El Niño Modoki has occurred frequently, which may cause the coupling position of SST and SSW to shift to the west of the equatorial Pacific in period 3 relative to period 2 in this study.

In addition, many scholars have used the Bjerknes stability index to estimate the overall linear ENSO stability, as well as the relative contribution of positive feedbacks and damping processes [21,41,42]. Kim and Jin found that many models of CMIP3 showed an increased sensitivity of oceanic dynamic response to wind forcing associated with the ENSO and surface wind response to anomalous SST forcing under global warming [21]. We speculate that the enhanced air–sea coupling in the key ENSO region may be related to changes in the sensitivity of the response between the ocean and atmosphere during 1955–2020.

In the decadal variation, the increase in the intensity of air–sea coupling seems to be related to the warming background, but whether this phenomenon can be found in the warming experiments of CMIP6 models, as well as its related mechanisms, requires further studies.

Author Contributions: Software, validation, formal analysis, investigation, resources, data curation, writing—original draft preparation, visualization, Z.L.; conceptualization, methodology, writing—review and editing, J.X. and Z.L.; supervision, project administration, funding acquisition, J.X. All authors have read and agreed to the published version of the manuscript.

Funding: This study was jointly supported by the National Natural Science Foundation of China (42130605), and the Guangdong Basic and Applied Basic Science Research Fundation (2019B1515120018) and Shenzhen Nature Science Foundation (JCYJ20210324131810029).

Institutional Review Board Statement: Not applicable.

Informed Consent Statement: Not applicable.

Data Availability Statement: The SST presented in this study can be found in the NOAA ERSST v5 at https://psl.noaa.gov/data/gridded/data.noaa.ersst.v5.html (accessed on 8 June 2022). The SLP of Tahiti station and Darwin station, as well as the Nino3.4 index are obtained from the NOAA Climate Prediction Center at https://origin.cpc.ncep.noaa.gov/data/indices/ (accessed on 8 June 2022). The NCEP/NCAR reanalysis version 1 data are available at https://psl.noaa.gov/data/gridded/data.ncep.reanalysis.html (accessed on 14 June 2022). The OHC data can be available in the Institute of Atmospheric Physics at http://www.ocean.iap.ac.cn/ (accessed on 15 April 2022). The ERA5 monthly averaged data on single levels can be found in the Copernicus Climate Change Service Climate Data Store at https://doi.org/10.24381/cds.f17050d7.

Conflicts of Interest: The authors declare no conflict of interest.

References

1. Fan, X.; Qin, Y.Y.; Gao, X. Interpretation of the main conclusions and suggestions of lPCC AR6 working group I report. *Environ. Prot* **2021**, *49*, 44–48. [CrossRef]
2. Lin, Y.; Franzke, C.L. Scale-dependency of the global mean surface temperature trend and its implication for the recent hiatus of global warming. *Sci. Rep.* **2015**, *5*, 12971. [CrossRef]
3. Dong, L.; McPhaden, M.J. The role of external forcing and internal variability in regulating global mean surface temperatures on decadal timescales. *Environ. Res. Lett.* **2017**, *12*, 034011. [CrossRef]
4. McPhaden, M.J.; Santoso, A.; Cai, W. Introduction to El Niño Southern Oscillation in a Changing Climate. In *El Niño Southern Oscillation in a Changing Climate*, 1st ed.; John Wiley & Sons: Hoboken, NJ, USA, 2020; pp. 1–19. [CrossRef]
5. Wang, B.; Wu, R.; Fu, X. Pacific–East Asian Teleconnection: How Does ENSO Affect East Asian Climate? *J. Clim.* **2000**, *13*, 1517–1536. [CrossRef]
6. McPhaden, M.J.; Zebiak, S.E.; Glantz, M.H. ENSO as an Integrating Concept in Earth Science. *Science* **2006**, *314*, 1740–1745. [CrossRef] [PubMed]
7. McPhaden, M.J.; Lee, T.; McClurg, D. El Niño and its relationship to changing background conditions in the tropical Pacific Ocean. *Geophys. Res. Lett.* **2011**, *38*, L15709. [CrossRef]
8. Ke, M.; Wang, Z.; Pan, W.; Luo, H.; Yang, S.; Guo, R. Extremely Strong Western Pacific Subtropical High in May 2021 Following a La Niña Event: Role of the Persistent Convective Forcing over the Indian Ocean. *Asia-Pac. J. Atmos. Sci.* **2022**, 1–12. [CrossRef]
9. Bjerknes, J. Atmospheric teleconnections from the equatorial Pacific. *Mon. Weather Rev.* **1969**, *97*, 163–172. [CrossRef]
10. Wang, C. A review of ENSO theories. *Natl. Sci. Rev.* **2018**, *5*, 813–825. [CrossRef]
11. Tang, Y.; Zhang, R.H.; Liu, T.; Duan, W.; Yang, D.; Zheng, F.; Ren, H.; Lian, T.; Gao, C.; Chen, D.; et al. Progress in ENSO prediction and predictability study. *Natl. Sci. Rev.* **2018**, *5*, 826–839. [CrossRef]
12. Yang, S.; Li, Z.; Yu, J.Y.; Hu, X.; Dong, W.; He, S. El Niño–Southern Oscillation and its impact in the changing climate. *Natl. Sci. Rev.* **2018**, *5*, 840–857. [CrossRef]
13. Chen, D.; Lian, T. Frontier of El Niño-Southern Oscillation research. *Chin. Sci. Bull.* **2020**, *65*, 4001–4003. [CrossRef]
14. Suarez, M.J.; Schopf, P.S. A delayed action oscillator for ENSO. *J. Atmos. Sci.* **1988**, *45*, 3283–3287. [CrossRef]
15. Collins, M.; An, S.I.; Cai, W.; Ganachaud, A.; Guilyardi, E.; Jin, F.F.; Jochum, M.; Lengaigne, M.; Power, S.; Timmermann, A.; et al. The impact of global warming on the tropical Pacific Ocean and El Niño. *Nat. Geosci.* **2010**, *3*, 391–397. [CrossRef]
16. Grothe, P.R.; Cobb, K.M.; Liguori, G.; Di Lorenzo, E.; Capotondi, A.; Lu, Y.; Cheng, H.; Edwards, R.L.; Southon, J.R.; Santos, G.M.; et al. Enhanced El Niño–Southern oscillation variability in recent decades. *Geophys. Res. Lett.* **2020**, *47*, e2019GL083906. [CrossRef]
17. Cai, W.; Santoso, A.; Collins, M.; Dewitte, B.; Karamperidou, C.; Kug, J.S.; Lengaigne, M.; McPhaden, M.J. Changing El Niño–Southern Oscillation in a warming climate. *Nat. Rev. Earth Environ.* **2021**, *2*, 628–644. [CrossRef]
18. Vecchi, G.A.; Soden, B.J.; Wittenberg, A.T.; Held, I.M.; Leetmaa, A.; Harrison, M.J. Weakening of tropical Pacific atmospheric circulation due to anthropogenic forcing. *Nature* **2006**, *441*, 73–76. [CrossRef]
19. Deng, L.; Yang, X.; Xie, Q. ENSO frequency change in coupled climate models as response to the increasing CO_2 concentration. *Chin. Sci. Bull.* **2010**, *55*, 744–751. [CrossRef]
20. Philip, S.; Van Oldenborgh, G.J. Shifts in ENSO coupling processes under global warming. *Geophys. Res. Lett.* **2006**, *33*, L11704. [CrossRef]
21. Kim, S.T.; Jin, F.F. An ENSO stability analysis. Part II: Results from the twentieth and twenty-first century simulations of the CMIP3 models. *Clim. Dynam.* **2011**, *36*, 1609–1627. [CrossRef]
22. Chen, L.; Li, T.; Yu, Y. Causes of strengthening and weakening of ENSO amplitude under global warming in four CMIP5 models. *J. Clim.* **2015**, *28*, 3250–3274. [CrossRef]
23. Cai, W.; Wang, G.; Dewitte, B.; Wu, L.; Santoso, A.; Takahashi, K.; Yang, Y.; Carréric, A.; McPhaden, M.J. Increased variability of eastern Pacific El Niño under greenhouse warming. *Nature* **2018**, *564*, 201–206. [CrossRef]
24. Xia, Y.; Sun, X.G.; Yan, Y.; Feng, W.Y.; Huang, F.; Yuan, X.Q. Change of ENSO characteristics in response to global warming. *Chin. Sci. Bull.* **2017**, *62*, 1738–1751. [CrossRef]

25. Huang, B.; Thorne, P.W.; Banzon, V.F.; Boyer, T.; Chepurin, G.; Lawrimore, J.H.; Menne, M.J.; Smith, T.M.; Vose, R.S.; Zhang, H.M. Extended reconstructed sea surface temperature, version 5 (ERSSTv5): Upgrades, validations, and intercomparisons. *J. Clim.* **2017**, *30*, 8179–8205. [CrossRef]
26. Climate Prediction Center—Monitoring & Data: Current Monthly Atmospheric and Sea Surface Temperatures Index Valuest. Available online: https://origin.cpc.ncep.noaa.gov/data/indices/ (accessed on 30 July 2022).
27. Kalney. The ncep/ncar 40-year reanalysis project. *Bull. Amer. Meteor. Soc.* **1996**, *74*, 789–799. [CrossRef]
28. Cheng, L.; Trenberth, K.E.; Fasullo, J.; Boyer, T.; Abraham, J.; Zhu, J. Improved estimates of ocean heat content from 1960 to 2015. *Sci. Adv.* **2017**, *3*, e1601545. [CrossRef]
29. Bretherton, C.S.; Smith, C.; Wallace, J.M. An intercomparison of methods for finding coupled patterns in climate data. *J. Clim.* **1992**, *5*, 541–560. [CrossRef]
30. Wallace, J.M.; Smith, C.; Bretherton, C.S. Singular value decomposition of wintertime sea surface temperature and 500-mb height anomalies. *J. Clim.* **1992**, *5*, 561–576. [CrossRef]
31. Wu, H.B.; Wu, L. *Methods for Diagnosing and Forecasting Climate Variability*, 1st ed.; Meteorological Press: Beijing, China, 2005; pp. 103–162.
32. Yang, X.; Zhu, Y.; Qian, X.; Ren, X.; Xu, G. Advances in studies of Pacific decadal oscillation. *Chin. J. Atmos. Sci.* **2004**, *28*, 979–992.
33. Kwon, M.; Yeh, S.W.; Park, Y.G.; Lee, Y.K. Changes in the linear relationship of ENSO–PDO under the global warming. *Int. J. Climatol.* **2013**, *33*, 1121–1128. [CrossRef]
34. Shi, Y.; Su, J. A new equatorial oscillation index for better describing ENSO and westerly wind bursts. *J. Meteorol. Res.* **2020**, *34*, 1025–1037. [CrossRef]
35. Xu, J.; Zhu, Q.; Shi, N. The interaction of East Asian winter monsoon with ENSO cycle and their interdecadal variations in last century. *Sci. Atmos. Sin.* **1997**, *21*, 648–657. [CrossRef]
36. Yeh, S.W.; Kug, J.S.; Dewitte, B.; Kwon, M.H.; Kirtman, B.P.; Jin, F.F. El Niño in a changing climate. *Nature* **2009**, *461*, 511–514. [CrossRef] [PubMed]
37. Chen, L.; Li, T.; Yu, Y.; Behera, S.K. A possible explanation for the divergent projection of ENSO amplitude change under global warming. *Clim. Dynam.* **2017**, *49*, 3799–3811. [CrossRef]
38. Behera, S.; Yamagata, T. Climate dynamics of ENSO Modoki phenomena. In *Oxford Research Encyclopedia of Climate Science*; Oxford University Press: New York, NY, USA, 2018. [CrossRef]
39. Ashok, K.; Behera, S.K.; Rao, S.A.; Weng, H.; Yamagata, T. El Niño Modoki and its possible teleconnection. *J. Geophys. Res.* **2007**, *112*, C11007. [CrossRef]
40. Kao, H.Y.; Yu, J.Y. Contrasting eastern-Pacific and central-Pacific types of ENSO. *J. Clim.* **2009**, *22*, 615–632. [CrossRef]
41. Lübbecke, J.F.; McPhaden, M.J. Assessing the twenty-first-century shift in ENSO variability in terms of the Bjerknes stability index. *J. Clim.* **2014**, *27*, 2577–2587. [CrossRef]
42. Kim, S.T.; Cai, W.; Jin, F.F.; Santoso, A.; Wu, L.; Guilyardi, E.; An, S.I. Response of El Niño sea surface temperature variability to greenhouse warming. *Nat. Clim. Chang.* **2014**, *4*, 786–790. [CrossRef]